Electron-phonon scattering effects on electronic and optical properties of orthorhombic GeS

Cesar E. P. Villegas,[1,2] A. R. Rocha,[2] and Andrea Marini[1,3]

[1]*Istituto di Struttura della Materia of the National Research Council, Via Salaria Km 29.3, I-00016 Monterotondo Stazione, Italy*

[2]*Instituto de Física Teórica, Universidade Estadual Paulista (UNESP), Rua Dr. Bento T. Ferraz, 271, São Paulo, SP 01140-070, Brazil*

[3]*European Theoretical Spectroscopy Facilities (ETSF), Via Salaria Km 29.3, I-00016 Monterotondo Stazione, Italy*

(Received 28 July 2016; published 19 October 2016)

Group-VI monochalcogenides are attracting a great deal of attention due to their peculiar anisotropic properties. Very recently, it has been suggested that GeS could act as a promissory absorbing material with high input-output ratios, which are relevant features for designing prospective optoelectronic devices. In this work, we use the *ab initio* many-body perturbation theory to study the role of electron-phonon coupling on orthorhombic GeS. We identify the vibrational modes that efficiently couple with the electronic states responsible for giving rise to the first and second excitonic state. We also study finite-temperature optical absorption, and we show that even at $T \to 0$ K, the role of the electron-phonon interaction is crucial to properly describe the position and width of the main experimental excitation peaks. Our results suggest that the electron-phonon coupling is essential to properly describe the optical properties of the monochalcogenides family.

DOI: 10.1103/PhysRevB.94.134306

I. INTRODUCTION

Layered materials have become prospective platforms for the next generation of technological devices due to their widely tunable physical properties [1,2]. Their potential applications include optoelectronic [3], photovoltaic [4,5], and thermoelectric [6,7] properties. Besides the well-characterized hexagonal layered crystals such as graphite [8], boron nitride [9,10], and transition-metal dichalcogenides [11,12], recently black phosphorus (BP) [13,14] and group-VI monochalcogenides (GeS, GeSe, SnSe, and SnS) [15,16] have gained renewed attention, fundamentally, as a direct consequence of their unique anisotropic properties. These layered materials possess an orthorhombic crystalline structure (*Pnma* space group) with a puckered atomic arrangement. This peculiarity gives rise to well-defined zigzag and armchair directions that are crucial in determining a number of interesting phenomena [6,17–21].

Orthorhombic GeS exhibits an optical gap of ∼1.65 eV [22] that, together with its low toxicity [23] and stability under normal conditions—superior to the one observed in BP [24,25]—represents an appealing candidate for optoelectronic applications. In fact, a recent report indicates that GeS-based photodetectors could provide high ratios of external quantum efficiency and detectivity that are comparable with the ones found in current commercial photodetectors [26]. In addition, it has been suggested that GeS could also have thermoelectric potential due to low values of thermal conductivity [7]. These potential applications, which are highly temperature-dependent, exhort to a comprehensive understanding of the finite-temperature properties of GeS.

While extensive experimental characterization of GeS, including optical measurements, has been carried out [22,27–30], *ab initio* calculations of its fundamental properties are still scarce. Despite the accurate prediction of GeS vibrational properties [28], the prediction of its optical spectrum still presents some discrepancies [15,31–33]. For instance, Makinistian and Albansi [31] studied the optical properties of GeS using different light polarizations and pressures. Nonetheless, the authors used advanced methodologies based on the Bethe-Salpeter equation (BSE) combined with many-body perturbation theory (MBPT), but their calculations failed to predict the relative exciton intensities and peak positions. This is likely a consequence of comparing their results with finite-temperature measurements. As a common feature, other state-of-the-art optical studies on GeS [15,32,33] consider atoms frozen in their equilibrium positions, thus neglecting the role of the electron-phonon (EP) interaction. Without including the EP interaction, temperature effects cannot be described. Even at $T \to 0$ K, the electronic states can be strongly renormalized by the quantum nature of atoms; this is the quantum zero-point motion (ZPM) effect [34,35].

From the discrepancies between experiments and current levels of theory, one can conclude that the electron-phonon (EP) coupling plays a nontrivial role in GeS. In addition, the EP coupling could also play an important role in the entire family of monochalcogenide crystals. This is supported by recent theoretical works addressing the finite-temperature effects of semiconductors through the inclusion of EP coupling [36–40].

In fact, it is well known that lattice vibrations can affect the optical properties of semiconductors leading to changes in the exciton peak position, linewidth, and selection rules [41–43]. Therefore, it is important to include temperature effects on the state-of-the-art simulations to better describe the optical properties and to elucidate the dynamics of the EP scattering mechanisms.

In this work, we provide a theoretical description of the effect of the EP coupling on the electronic and optical properties of orthorhombic GeS. We clearly identify the most important phonon modes that efficiently couple with the electronic states responsible for giving rise to the first and second excitonic states. Our results show that, at the band edge, the infrared longitudinal B_{2u} mode is the main scattering source for the electronic states. This mode also couples efficiently with the first excitonic state. In contrast, the electronic states giving rise to the second excitonic state couple mostly with modes A_g^1 and B_{3g}^2. We also calculate the finite-temperature optical absorption, and we show that even at $T \to 0$ K, the role of EP coupling is crucial to better describe the absorption linewidth and exciton peak positions.

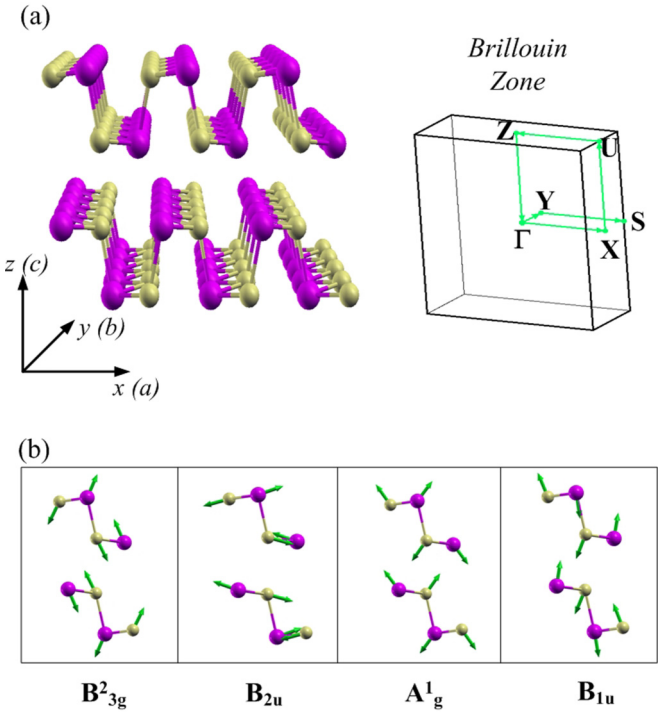

FIG. 1. (a) Schematic representation of the crystal structure and Brillouin zone of orthorhombic GeS showing the main crystallographic directions. (b) Representative atomic vibrations of GeS. The Mulliken notation for the vibrational modes is chosen because they resemble black phosphorus vibrational modes.

II. THEORY AND METHODOLOGY

We consider a pristine GeS crystal as shown in Fig. 1(a). It consists of a layered puckered structure containing eight atoms in the orthorhombic unit cell for which each Ge atom is bonded to three S atoms. The obtained fully relaxed lattice parameters ($a = 4.30$ Å, $b = 3.67$ Å, and $c = 10.63$ Å) are in good agreement with experimental ones [28].

Our study is conducted in three steps. First, plane-wave density functional theory is used to obtain the electronic ground state. The Perdue-Burke-Ernzerhof (PBE) exchange-correlation potential including van der Waals corrections within the semiempirical dispersion scheme (PBE-D) is used. We employed norm-conserving pseudopotentials, a 60 Ry kinetic energy cutoff, and a k-sampling grid in the Monkhorst-Pack scheme of $8 \times 8 \times 4$ as implemented in the QUANTUM ESPRESSO code [44]. The structures were fully optimized to their equilibrium position with forces smaller than 0.002 eV/Å.

Next, we use density functional perturbation theory (DFPT) [45] to compute the vibrational frequencies $\omega_{\mathbf{q}\lambda}$ and the derivatives of the self-consistent Kohn-Sham potential with respect to the atomic displacements needed to evaluate the electron-phonon coupling matrix elements.

Many-body perturbation theory (MBPT) [46] is used to describe the temperature dependent electronic states. There, the electron-phonon interaction is treated perturbatively [47,48] by considering the first- and second-order Taylor expansion in the nuclear displacement, commonly known as the Fan and Debye-Waller (DB) terms, respectively. The corresponding interacting Green's function, whose poles define the quasiparticle excitations, can be written as

$$G_{n\mathbf{k}}(\omega,T) = \left[\omega - \epsilon_{n\mathbf{k}} - \Sigma^{\mathrm{Fan}}_{n\mathbf{k}}(\omega,T) - \Sigma^{\mathrm{DW}}_{n\mathbf{k}}(T)\right]^{-1}, \quad (1)$$

where $\epsilon_{n\mathbf{k}}$ is the Kohn-Sham ground-state eigenenergies for frozen atoms. Σ^{Fan} is the Fan contribution

$$\Sigma^{\mathrm{Fan}}_{n\mathbf{k}}(i\omega,T) = \sum_{n'\mathbf{q}\lambda} \frac{|g^{\mathbf{q}\lambda}_{nn'\mathbf{k}}|^2}{N}\left[\frac{N_{\mathbf{q}\lambda}(T) + 1 - f_{n'\mathbf{k}-\mathbf{q}}}{i\omega - \epsilon_{n'\mathbf{k}-\mathbf{q}} - \omega_{\mathbf{q}\lambda}} + \frac{N_{\mathbf{q}\lambda}(T) + f_{n'\mathbf{k}-\mathbf{q}}}{i\omega - \epsilon_{n'\mathbf{k}-\mathbf{q}} + \omega_{\mathbf{q}\lambda}}\right], \quad (2)$$

and Σ^{DW} is the Debye-Waller term,

$$\Sigma^{\mathrm{DW}}_{n\mathbf{k}}(T) = -\frac{1}{2}\sum_{n'\mathbf{q}\lambda} \frac{\Lambda^{\mathbf{q}\lambda}_{nn'\mathbf{k}}}{N}\left[\frac{2N_{\mathbf{q}\lambda}(T)+1}{\epsilon_{n\mathbf{k}} - \epsilon_{n'\mathbf{k}}}\right]. \quad (3)$$

Here $N_{\mathbf{q}\lambda}$ and $f_{n'\mathbf{k}-\mathbf{q}}$ represent the Bose-Einstein and Fermi-Dirac distribution functions, while N is the number of $\mathbf{q}$ points in the Brillouin zone. This last $\mathbf{q}$-mesh is taken randomly to better map out the phonon transferred momentum [49]. We include 200 electronic bands and 60 random $\mathbf{q}$-points for the phonon momentum to evaluate Eqs. (2) and (3).

The electron-phonon coupling matrix elements $g^{\mathbf{q}\lambda}_{nn'\mathbf{k}}$, which represent the probability amplitude for an electron to be scattered due to emission or absorption of phonons, is given by

$$g^{\mathbf{q}\lambda}_{nn'\mathbf{k}} = \sum_{s\alpha}[2M_s\omega_{\mathbf{q}\lambda}]^{-1/2} e^{i\mathbf{q}\cdot\tau_s}\xi_\alpha(\mathbf{q}\lambda|s) \times \langle n'\mathbf{k}-\mathbf{q}|\frac{\partial V_{\mathrm{scf}}(\mathbf{r})}{\partial R_{s\alpha}}|n\mathbf{k}\rangle, \quad (4)$$

where M_s is the atomic mass of the sth atom, τ_s is the position of the atomic displacement in the unit cell, $\xi_\alpha(\mathbf{q}\lambda|s)$ are the components of the phonon polarization vectors, and $V_{\mathrm{scf}}(\mathbf{r})$ is the self-consistent DFT ionic potential. The second-order electron-phonon matrix elements are given by

$$\Lambda^{\mathbf{q}\lambda,\mathbf{q}'\lambda'}_{nn'\mathbf{k}} = \frac{1}{2}\sum_s\sum_{\alpha\beta}\frac{\xi^*_\alpha(\mathbf{q}\lambda|s)\xi_\alpha(\mathbf{q}'\lambda'|s)}{2M_s[\omega_{\mathbf{q}\lambda}\omega_{\mathbf{q}'\lambda'}]^{1/2}} \times \langle n'\mathbf{k}-\mathbf{q}-\mathbf{q}'|\frac{\partial^2 V_{\mathrm{scf}}(\mathbf{r})}{\partial R_{s\alpha}\partial R_{s\beta}}|n\mathbf{k}\rangle. \quad (5)$$

Equation (5) is rewritten, using translational invariance, in terms of the first-order gradients only (see Refs. [47] and [48]).

The EP quasiparticle corrections to the Kohn-Sham eigenenergies are calculated within the quasiparticle approximation (QPA). It consists in expanding, to first order, the self-energy frequency dependence around the bare energies. In this way, one can write the temperature-dependent EP electronic states as [50]

$$E_{n\mathbf{k}}(T) \approx \epsilon_{n\mathbf{k}} + Z_{n\mathbf{k}}(T)\left[\Sigma^{\mathrm{Fan}}_{n\mathbf{k}}(\epsilon_{n\mathbf{k}},T) + \Sigma^{\mathrm{DW}}_{n\mathbf{k}}(T)\right], \quad (6)$$

where $Z_{n\mathbf{k}}(T) = [1 - \frac{\partial\,\mathrm{Re}\Sigma^{\mathrm{Fan}}_{n\mathbf{k}}(\omega)}{\partial\omega}|_{\omega=\epsilon_n}]^{-1}$ is the renormalization factor. Given that the Fan self-energy term is a complex function, it provides both the energy renormalization shift and the intrinsic quasiparticle lifetime.

The renormalization factor can be interpreted as the quasiparticle charge, and it constitutes a useful tool to assess the validity of the QPA; the closer $Z_{n\mathbf{k}}$ is to 1, the more appropriate is the QPA. In fact, by assuming the validity of the QPA, one is able to rewrite Eq. (1) as

$$G_{n\mathbf{k}} = \frac{Z_{n\mathbf{k}}}{\omega - E_{n\mathbf{k}}(T)}, \tag{7}$$

whose spectral function (SF), $A_{n\mathbf{k}} = \pi^{-1}\mathrm{Im}[G_{n\mathbf{k}}]$, should resemble a Lorentzian function centered at $E_{n\mathbf{k}}$. As the lattice vibrations become stronger, the SF gets wider and extends over large energy windows. Note, however, that one should be aware of the breakdown of the QPA that can be recognized by asymmetries and the appearance of new peaks in the SF [38,51,52].

Finally, the temperature-dependent excitonic effects are included on top of the frozen-atom Bethe-Salpeter equation (BSE),

$$L_{\mathbf{K}_1\mathbf{K}_2}(\omega) = L^0_{\mathbf{K}_1\mathbf{K}_2}(\omega) + L^0_{\mathbf{K}_1\mathbf{K}_3}(\omega)\Xi_{\mathbf{K}_3\mathbf{K}_4}L_{\mathbf{K}_4\mathbf{K}_2}(\omega), \tag{8}$$

by considering the temperature-dependent noninteracting electron-hole Green's function [37],

$$L^0_{\mathbf{K}_1\mathbf{K}_2}(\omega,T) = \left[\frac{f_{c_1\mathbf{k}_1} - f_{v_1\mathbf{k}_1}}{\omega - E_{c_1\mathbf{k}_1}(T) - E_{v_1\mathbf{k}_1}(T) + 0^+}\right]\delta_{\mathbf{K}_1\mathbf{K}_2}. \tag{9}$$

Here $\mathbf{K} = (c,v,\mathbf{k})$ comprises the electronic band index and $\Xi = i(W - V)$ represents the BSE kernel composed by the difference between the static screened and bare Coulomb potential. We adopt a static BSE kernel to describe excitonic effects following Refs. [53] and [54] that have shown its accuracy in predicting optical properties in solids. By solving Eq. (8) with the temperature-dependent propagator, the frozen atom BSE Hamiltonian becomes non-Hermitian due to the presence of imaginary QP energies $E_{n\mathbf{k}}$. This is crucial for computing the optical absorption since it provides an intrinsic exciton-phonon linewidth, which removes the need to include an artificial broadening. Note that the electron-electron induced linewidths are disregarded in the present case since, as previously shown [55,56], their contributions in semiconductors are zero for energy windows $2E_g$ close to the CBM and VBM. The BSE is calculated by considering 720 bands and a 22 Ry energy cutoff in the screened electron-hole potential. The optical absorption is computed with the YAMBO code [50] using a fine grid with 24 000 random $\mathbf{k}$-points with seven valence and seven conduction bands in the *e-h* kernel. The parameter 0^+ in Eq. (9) is set to 5 meV for numerical reasons.

III. RESULTS

We begin our study by describing the electronic structure shown in Fig. 2(a) using PBE. There, we observe an indirect band gap of ∼1.16 eV, whose valence-band maximum (VBM) is located at around three-fifths of the ΓX path, while the conduction-band minimum (CBM) is at Γ. In Fig. 2(b) we show the k-resolved density of states projected on Ge and S atoms. Overall, the valence (conduction) states are dominated by S (Ge) atoms mostly with p-type contributions. These results are consistent with previous theoretical predictions [33,57].

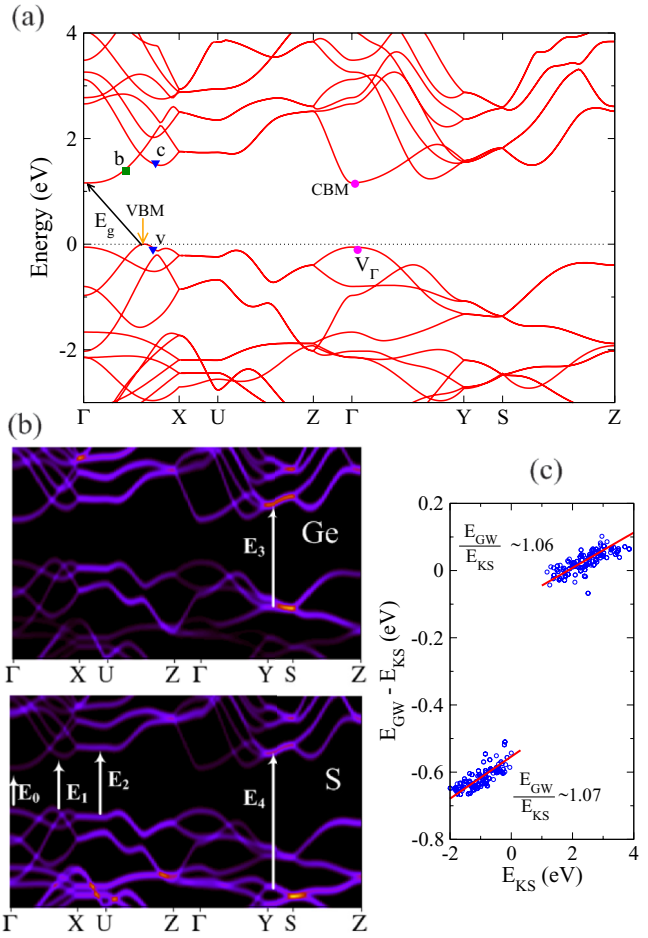

FIG. 2. (a) Electronic band structure of GeS showing the indirect band gap. Blue dots represent the wave vector at which the excitonic state E_1 takes place while V_Γ and CBM are the ones associated with the exciton state E_0. (b) k-resolved projected density of states for Ge and S atom contributions. White arrows indicates the wave vector of the most probable transitions for light polarized in the x direction. (c) Quasiparticle energy corrections as a function of Kohn-Sham energy states showing the renormalization trend. Red lines represent a linear fit of the data.

Note that the direct gap at Γ is only 50 meV larger than the indirect gap. The oscillator strength reveals that the first excitonic state E_0 is located at Γ, whereas the wave-vector number of the second excitonic state E_1 occurs from points v to c depicted in Fig. 2(a). Due to the importance of these optical transitions, our EP coupling study will be conducted at these wave-vector numbers. A schematic representation of the relevant optical transitions in GeS is shown in Fig. 2(b).

To properly describe the excitonic effects on the optical properties, one requires a good description of the electronic band gap. Thus, we calculate the quasiparticle (QP) corrections within the G_0W_0 approach and plot them as a function of the GGA eigenenergies in Fig. 2(c). We obtained a QP correction of 0.58 eV at Γ, which results in a QP gap of ≈1.79 eV. This is consistent with previous GW calculations [57]. We also note that the QP corrections are slightly dispersive with respect to the GGA eigenenergies. In fact, by fitting the QP corrections data to a linear curve, we found that the conduction

and valence bands are, on average, slightly stretched by 6% and 7%, respectively. These findings are important since the QP correction at Γ and the average stretching of the bands are taken into account in the form of a scissor operator to formally solve Eq. (8). Notice that 720 bands and an energy cutoff of 18 Ry for the response function are included for evaluating the G_0W_0 corrections.

We proceed with the study of the EP scattering mechanisms. Toward that end, we compute the generalized Eliashberg function

$$g^2F_{n\mathbf{k}}(\omega) = \frac{1}{N}\sum_{n'\mathbf{q}\lambda}\left[\frac{|g^{\mathbf{q}\lambda}_{nn'\mathbf{k}}|^2}{\epsilon_{n\mathbf{k}} - \epsilon_{n'\mathbf{k}-\mathbf{q}}} - \frac{1}{2}\frac{\Lambda^{\mathbf{q}\lambda}_{nn'\mathbf{k}}}{\epsilon_{n\mathbf{k}} - \epsilon_{n'\mathbf{k}}}\right]\delta(\omega-\omega_{\mathbf{q}\lambda}), \tag{10}$$

which enables us to visualize the EP coupling strength for a given state $|n\mathbf{k}\rangle$. We defined the band-edge Eliashberg function as $F_{\mathrm{BE}} = F_{c_i} - F_{v_i}$, where the subindex c_i (v_i) refers to a given conduction (valence) state. This function provides useful information regarding the vibrational modes that eventually couple with an excitonic state rising at the same wave-vector numbers.

In Fig. 3(a), we show the Eliashberg function at Γ for the highest valence state (V_Γ) and CBM, the wave vectors associated with the exciton state E_0. At high frequencies, F_{BE} present two dominant peaks spanning from 285 to 320 cm^{-1} that result mainly from scattering events at V_Γ. For frequencies below the phonon dispersion gap, the most important contributions cover the range from 50 to 140 cm^{-1}. In Figs. 3(d) and 3(e) we project F_{BE} on each mode. For simplicity, only the most representative modes are shown. Some of these modes are schematically represented in Fig. 1(b).

For frequencies below 90 cm^{-1}, the electronic states couple mostly with the acoustic modes (AM) and with less intensity to the shear modes (SM). Notice that, in contrast to black phosphorus [21], F_{BE} present non-negligible negative contributions for frequencies below 50 cm^{-1}, which guarantees the reduction of the band gap as the temperature increases, a feature observed in experiments [27]. Given that

$$\Delta E_g(T) \propto \int d\omega\, g^2F_{\mathrm{BE}}(\omega)[N_{\mathbf{q}\lambda}(T) + 1/2], \tag{11}$$

the Bose-Einstein distribution will always weigh more heavily on the low-frequency region where F_{BE} is negative, thus causing the monotonic decreases of the band gap with the temperature.

At higher frequencies, the dominant EP peaks are mostly attributed to modes B_{2u} and B^2_{3g}, with B_{2u} providing the most intense contribution, as shown in Fig. 3(e). Based on this information, one should expect that the first excitonic state E_0 couples efficiently with the infrared longitudinal mode B_{2u}.

Moreover, in Fig. 3(c) we show the EP coupling at (v) and (c) states, whose wave-vector numbers give rise to the exciton state E_1. In contrast to the previous case, we note a significant enhancement of the EP strength around 250 cm^{-1}, which results from the EP scattering events at the c state. In Fig. 3(f) we show the projection of F_{BE} onto the high-frequency optical modes. It clearly shows that the electrons interact more strongly with mode B^2_{3g}. Moreover, the coupling of electrons

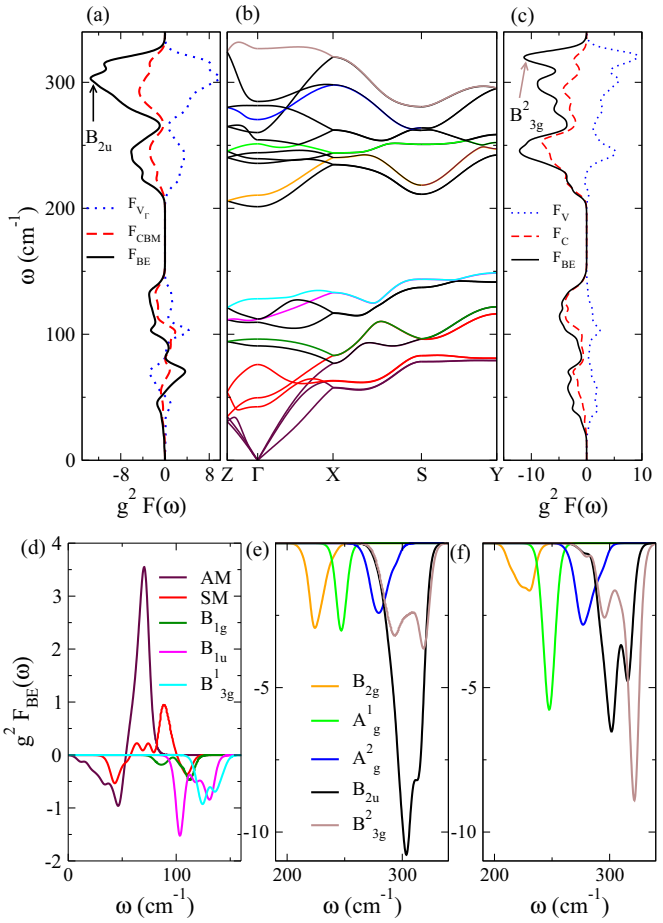

FIG. 3. (a) Generalized electron-phonon Eliashberg function for V_Γ (blue dotted line), CBM (red dot-dashed line), and band edge (black solid line). (b) GeS phonon dispersion along selected symmetry points. (c) Eliashberg function at wave vectors **c** and **v**, which give rise to the excitonic state E_1. The band-edge Eliashberg function, related to V_Γ and CBM, projected on phonon modes with frequencies (d) below 200 cm^{-1} and (e) above 200 cm^{-1}. (f) Projected band-edge Eliashberg function, related to v and c wave-vector numbers. Only the most representative phonon modes are considered for simplicity. The curves for acoustic and shear mode curves comprise the contribution of three modes.

with mode A^1_g is considerably enhanced with respect to the excitonic state E_0. Therefore, the exciton state E_1 should couple with the vibrational modes A^1_g, B^2_{3g}, and B_{2u}, which in turn will be responsible for the subsequent reduction of the peak intensity and linewidth increase of the optical absorption.

From Eq. (6) in the limit $T \to 0$, we estimate the ZPM gap renormalization of $\approx -43 \pm 3$ meV at Γ, which is more than twice the value found in bulk black phosphorus [21]. It should be mentioned that despite the similar orthorhombic crystal structure between BP and GeS, the dominant EP scattering processes at the band edge of BP are the acoustical, A^2_g, and B_{2u} modes [21,58].

As previously stated, the MBPT approach allows us to take into account dynamical effects. Contrary to the single-particle description in which the states hold infinite lifetimes, the QP picture provides finite lifetimes in the form of the width of a Lorentzian curve centered at $E_{n\mathbf{k}}(T)$.

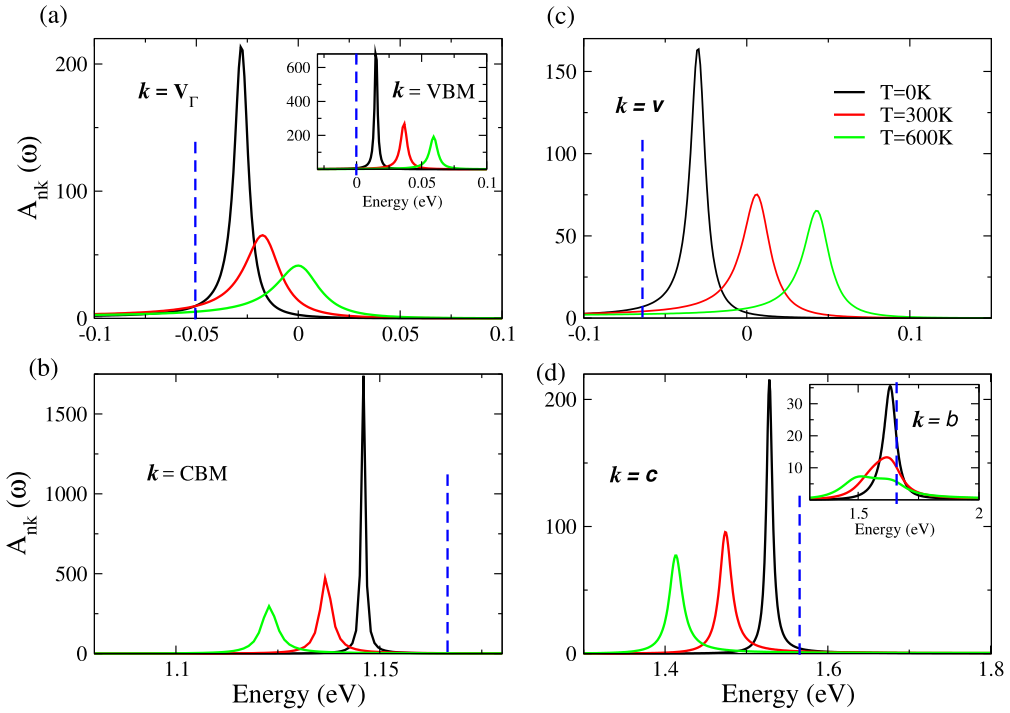

FIG. 4. Quasiparticle spectral function, $A_{n\mathbf{k}} = \pi^{-1}\mathrm{Im}[G_{n\mathbf{k}}]$, for (a) V_Γ and (b) CBM states. The SF for (c) valence state **v** and (d) conduction state **c**, responsible for the excitonic state E_1. The insets in (a) and (d) show the SF for wave vectors VBM and b, respectively, which are indicated in Fig. 1(c). In particular, the wave vector $k = b$ presents signatures associated with the quasiparticle breakdown.

In Figs. 4(a) and 4(b), we show the SFs related to the V_Γ and CBM states for different temperatures. The dashed blue lines depict the single-particle (Kohn-Sham) energy with an associated infinite lifetime. At $T = 0$ K, the SFs present a Lorentzian shape which is particularly sharp at the CBM, reflecting the long QP lifetimes. As the temperature increases, the linewidth gets broader and the SF peaks are redshifted (blueshifted) for CBM (V_Γ). This shift is a signature of the shrinking of the energy gap as the temperature increases. For completeness, the inset in Fig. 4(a) shows the SF at VBM, which follows similar trends to V_Γ.

Analogously, in Figs. 4(c) and 4(d) we show the SF of the states responsible for the exciton state E_1. We observe similar features as in the previous case regarding the temperature dependence. Note that the SFs keep their symmetric Lorentzian shape, which is a signature of the validity of the QP picture. To further discuss this, in the inset of Fig. 4(d) we show the SF of an arbitrary point in the conduction band [labeled as b in Fig. 2(a)]. At $T = 0$ K, we observe a broad Lorentzian curve that, as the temperature increases, becomes highly asymmetric. For $T = 600$ K, one can clearly see the formation of a second peak (a new state). The new state cannot be interpreted as a new electron-phonon state. In fact, it has been suggested that the appearances of new states are virtual transitions arising due to energy conservation, and they constitute a clear signature of the quasiparticle breakdown [34,51].

Finally, we explore the role of the EP interaction on the optical absorption and the relation between our calculations and experimental results. In Figs. 5(a) and 5(d), we present the imaginary part of the dielectric function at $T = 0$ K for light polarized in the x and y direction, respectively. The purple (blue) lines show the spectra with (without) EP contribution. Note that even at $T = 0$ K, the region close to the band edge of the absorption naturally gains a width. Also, the positions of the peaks including EP corrections are slightly redshifted as a consequence of the ZPM renormalization. In addition, even with the choice of a dense k-grid, the absorption without EP contribution shows spiky features over the entire energy range. This result clearly highlights the crucial role of including EP interactions for describing the optical properties of GeS, even at $T = 0$ K.

In Figs. 5(b) and 5(c), we show the finite-temperature absorption for x-polarized light. We clearly observe the natural smoothness of the theoretical curves that describe nicely the position of the peaks and their corresponding linewidths without using any external parameter. For instance, experimental results by Logothetidis *et al.* [27] estimated the position of the E_1 peak at 2.127 and 2.087 eV for $T = 84$ and 215 K, respectively. Our theoretical calculations locate the same peak at 2.128 and 2.096 eV, in excellent agreement. We summarized the energy position of the relevant transitions in Table I. Notice that as the temperature increases, the linewidths of our results deviate from the experimental ones, especially for the case of light polarized in the y direction. We argue that the reason for such deviation might be related to the accurate description of electronic states entering in Eq. (9). Indeed, by inspecting Eqs. (2) and (3), we realized that the energy dispersion curvature can affect considerably the results, especially the broadening. Thus, a considerable improvement of the EP lifetimes could be achieved by computing the EP coupling on top of G_0W_0 electronic structure [60]. However, this procedure is at this point computationally demanding, and thus it is not performed in this work. Despite this drawback, overall our GGA results predict fairly well the

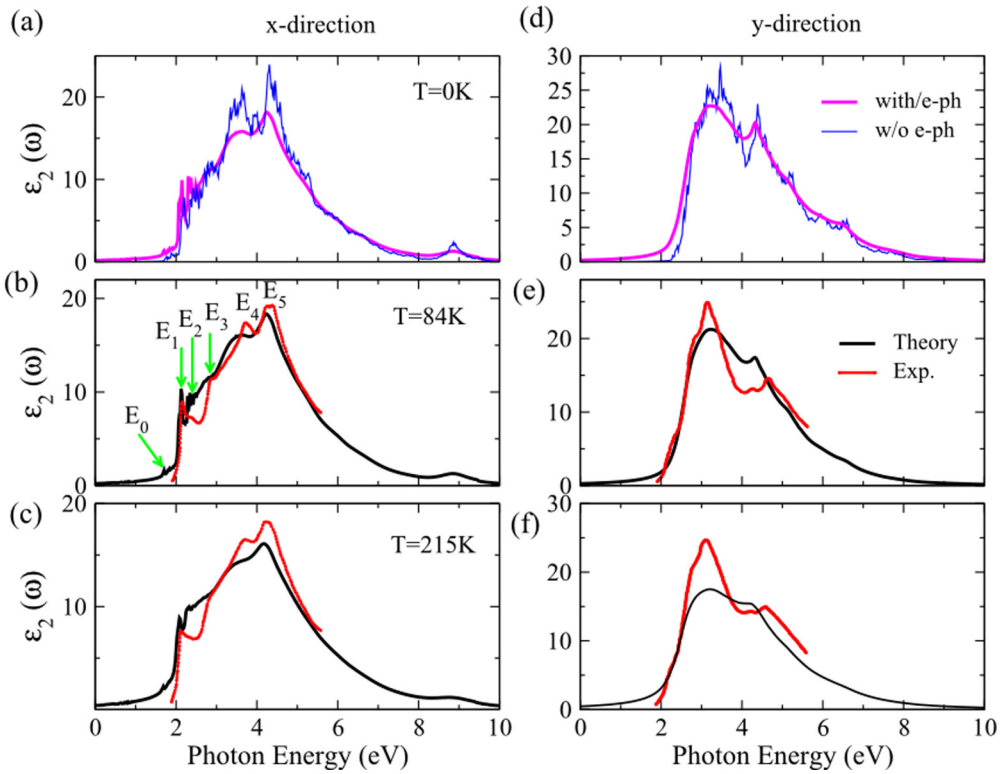

FIG. 5. Imaginary part of the dielectric function for different light polarizations. Purple and blue lines represent the theoretical prediction with and without EP corrections, respectively. Red dots are experimental results for different temperatures extracted from Ref. [27].

optical properties of GeS, especially for x-polarized light. Given the resemblance of the selection rules, band structures, and optical absorption curves [22,31] among the group-VI monochalcogenides, one can expect that, indeed, the EP coupling could play an important role for the description of the optical properties of this entire family.

Finally, we would like to mention that in few-layer and single-layer GeS forms, one would also expect a monotonic reduction of the band gap with the temperature. This can be ascribed to the resemblance of our phonon dispersion results for lower frequencies—the ones responsible for the gap temperature dependence slope—to recent vibrational studies in monolayer GeS [61]. Moreover, due to the reduced screening in the few-layer forms, the EP and exciton-phonon coupling might be enhanced, especially for optical modes.

TABLE I. Representative optical interband transitions energies in GeS at different temperatures for light polarized in the x direction. The values are expressed in eV. The experimental values for temperatures below 215 K are taken from Ref. [27], while those for 300 K are from Ref. [59].

	$T = 0$ K		$T = 84$ K		$T = 215$ K		$T = 300$ K	
	Theory	Expt.	Theory	Expt.	Theory	Expt.	Theory	Expt.
E_0	1.702		1.69		1.68		1.66	1.65 [22]
E_1	2.143	2.144	2.128	2.127	2.096	2.087	2.06	2.037
E_4	3.64	3.70	3.65	3.695	3.62	3.657	3.58	3.628
E_5	4.225	4.193	4.224	4.162	4.18	4.089	4.09	4.031

IV. CONCLUSIONS

We provided a theoretical description of the electron-phonon coupling effects on the electronic and optical properties of orthorhombic GeS based on *ab initio* many-body perturbation theory. Our results show that, at the band edge, the longitudinal mode B_{2u} couples efficiently with the electronic states. In addition, the electronic states that give rise to the exciton E_1 couple mostly with the vibrational modes A_g^1 and B_{3g}^2. Our results for the optical absorption show that even at $T \to 0$ K, the role of EP coupling is crucial to properly describe the absorption linewidths and peak positions. Our findings suggest that in order to properly describe group-VI monochalcogenides, one should include the electron-phonon interaction effects.

ACKNOWLEDGMENTS

C.E.P.V. acknowledges A. Molina-Sánchez for fruitful discussions and the financial support from the Brazilian agency FAPESP Grants No. 2015/14899-0 and No. 2012/24227-1. A.M. acknowledges the funding received from the *Futuro in Ricerca* Grant No. RBFR12SW0J of the Italian Ministry of Education, University and Research MIUR, the European Union project MaX *Materials design at the eXascale* H2020-EINFRA-2015-1, Grant Agreement No. 676598 and

Nanoscience Foundries and Fine Analysis–Europe H2020-INFRAIA-2014-2015, Grant Agreement No. 654360. A.R.R. acknowledges support from ICTP-SAIRF (FAPESP project 2011/11973-4) and the ICTP and the Simons Foundation for providing the opportunity to undertake this research by supporting his visit (to the ICTP) as an ICTP - Simons Associate. This work uses the computational resources from GRID-UNESP and CENAPAD/SP.

[1] A. K. Geim and I. V. Grigorieva, Nature (London) **499**, 419 (2013).
[2] H. Wang, F. Liu, W. Fu, Z. Fang, W. Zhoue, and Z. Liu, Nanoscale **6**, 12250 (2014).
[3] M. Buscema, J. O. Island, D. J. Groenendijk, S. I. Blanter, G. A. Steele, H. S. J. van der Zanta, and A. Castellanos-Gomez, Chem. Soc. Rev. **44**, 3691 (2015).
[4] M. M. Furchi, A. Pospischil, F. Libisch, J. Burgdörfer, and T. Mueller, Nano Lett. **14**, 4785 (2014).
[5] L. Britnell, R. M. Ribeiro, A. Eckmann, R. Jalil, B. D. Belle, A. Mishchenko, Y.-J. Kim, R. V. Gorbachev, T. Georgiou, S. V. Morozov, A. N. Grigorenko, A. K. Geim, C. Casiraghi, A. H. C. Neto, and K. S. Novoselov, Science **340**, 1311 (2013).
[6] L.-D. Zhao, S.-H. Lo, Y. Zhang, H. Sun, G. Tan, C. Uher, C. W. V. P. Dravid, and M. G. Kanatzidis, Nature (London) **508**, 373 (2014).
[7] G. Ding, G. Gao, and K. Yao, Sci. Rep. **5**, 9567 (2015).
[8] R. Senguptaa, M. Bhattacharyaa, S. Bandyopadhyayb, and A. K. Bhowmick, Prog. Polym. Sci. **36**, 638 (2011).
[9] R. T. Paine and C. K. Narula, Chem. Rev. **90**, 73 (1990).
[10] A. Pakdel, Y. Bandoa, and D. Golberg, Chem. Soc. Rev. **43**, 934 (2014).
[11] D. Jariwala, V. K. Sangwan, L. J. Lauhon, T. J. Marks, and M. C. Hersam, ACS Nano **8**, 1102 (2014).
[12] Q. H. Wang, K. Kalantar-Zadeh, A. Kis, J. N. Coleman, and M. S. Strano, Nat. Nanotech. **7**, 699 (2012).
[13] A. Castellanos-Gomez, J. Phys. Chem. Lett. **6**, 4280 (2015).
[14] X. Ling, H. Wang, S. Huang, F. Xia, and M. S. Dresselhaus, Proc. Natl. Acad. Sci. (U.S.A.) **112**, 4523 (2015).
[15] L. C. Gomes and A. Carvalho, Phys. Rev. B **92**, 085406 (2015).
[16] A. K. Singh and R. G. Hennig, Appl. Phys. Lett. **105**, 042103 (2014).
[17] H. B. Ribeiro, C. E. P. Villegas, D. A. Bahamon, D. Muraca, A. H. Castro-Neto, E. A. T. de Souza, A. R. Rocha, M. A. Pimenta, and C. J. S. de Matos, Nat. Commun. **7**, 12191 (2016).
[18] C. E. P. Villegas, A. Rodin, A. Carvalho, and A. R. Rocha, Phys. Chem. Chem. Phys. **18**, 27829 (2016).
[19] F. Xia, H. Wang, and Y. Jia, Nat. Commun. **5**, 4458 (2014).
[20] G. Qin, Z. Qin, W.-Z. Fang, L.-C. Zhang, S.-Y. Yue, Q.-B. Yan, M. Hu, and G. Su, Nanoscale **8**, 11306 (2016).
[21] C. E. P. Villegas, A. R. Rocha, and A. Marini, Nano Lett. **16**, 5095 (2016).
[22] R. Eymard and A. Otto, Phys. Rev. B **16**, 1616 (1977).
[23] N. Latiff, W. Z. Teo, Z. Sofer, S. Huber, A. C. Fisherc, and M. Pumera, RSC Adv. **5**, 67485 (2015).
[24] N. M. Lattif, W. Z. Teo, Z. Sofer, A. C. Fisher, and M. Pumera, Chem. Eur. J. **21**, 13991 (2015).
[25] A. Favron, E. Gaufrès, F. Fossard, A.-L. Phaneuf-L'Heureux, N. Y.-W. Tang, P. L. Lévesque, A. Loiseau, R. Leonelli, S. Francoeur, and R. Martel, Nat. Mater. **14**, 826 (2015).
[26] R. K. Ulaganathan, Y.-Y. Lu, C.-J. Kuo, S. R. Tamalampudi, R. Sankar, K. M. Boopathi, A. Anand, K. Yadavm, R. J. Mathew, C.-R. Liu, F. C. Choue, and Y.-T. Chen, Nanoscale **8**, 2284 (2016).
[27] S. Logothetidis, P. Lautenschlager, and M. Cardona, Phys. Rev. B **33**, 1110 (1986).
[28] H. C. Hsueh, M. C. Warren, H. Vass, G. J. Ackland, S. J. Clark, and J. Crain, Phys. Rev. B **53**, 14806 (1996).
[29] V. Cháb and I. Bartos, Phys. Status Solidi B **121**, 301 (1984).
[30] A. L. F. Lukes and E. Schmidt, Phys. Status Solidi B **39**, 921 (1981).
[31] L. Makinistian and E. A. Albanesi, Comput. Mater. Sci. **50**, 2872 (2011).
[32] B. R. Tuttle, S. M. Alhassan, and S. T. Pantelides, Phys. Rev. B **92**, 235405 (2015).
[33] L. Makinistian and E. A. Albanesi, Phys. Rev. B **74**, 045206 (2006).
[34] E. Cannuccia and A. Marini, Phys. Rev. Lett. **107**, 255501 (2011).
[35] F. Giustino, S. G. Louie, and M. L. Cohen, Phys. Rev. Lett. **105**, 265501 (2010).
[36] H. Kawai, K. Yamashita, E. Cannuccia, and A. Marini, Phys. Rev. B **89**, 085202 (2014).
[37] A. Marini, Phys. Rev. Lett. **101**, 106405 (2008).
[38] A. Molina-Sánchez, M. Palummo, A. Marini, and L. Wirtz, Phys. Rev. B **93**, 155435 (2016).
[39] M. Zacharias, C. E. Patrick, and F. Giustino, Phys. Rev. Lett. **115**, 177401 (2015).
[40] S. Poncé, Y. Gillet, J. L. Janssen, A. Marini, M. Verstraete, and X. Gonze, J. Chem. Phys. **143**, 102813 (2015).
[41] M. Cardona and M. L. W. Thewalt, Rev. Mod. Phys. **77**, 1173 (2005).
[42] P. Y. Yu and M. Cardona, *Fundamentals of Semiconductors* (Springer-Verlag, Berlin, 2010).
[43] S. Shokhovets, F. Barwolf, G. Gobsch, E. Runge, K. Köhler, and O. Ambacher, Phys. Status Solidi C **11**, 297 (2014).
[44] P. Giannozzi, *et al.*, J. Phys.: Condens. Matter **21**, 395502 (2009).
[45] S. Baroni, S. de Gironcoli, A. D. Corso, and P. Giannozzi, Rev. Mod. Phys. **73**, 515 (2001).
[46] G. Onida, L. Reining, and A. Rubio, Rev. Mod. Phys. **74**, 601 (2002).
[47] S. Poncé, G. Antonius, Y. Gillet, P. Boulanger, J. Laflamme Janssen, A. Marini, M. Côté, and X. Gonze, Phys. Rev. B **90**, 214304 (2014).
[48] A. Marini, S. Poncé, and X. Gonze, Phys. Rev. B **91**, 224310 (2015).
[49] S. Poncé, G. Antonius, P. Boulanger, E. Cannuccia, A. Marini, M. Côté, and X. Gonze, Comput. Mater. Sci. **83**, 341 (2014).
[50] A. Marini, C. Hogan, M. Grüning, and D. Varsano, Comput. Phys. Commun. **180**, 1392 (2009).

[51] E. Cannuccia and A. Marini, Eur. Phys. J. B **85**, 320 (2012).
[52] A. Gali, T. Demján, M. Vörös, G. Thiering, E. Cannuccia, and A. Marini, Nat. Commun. **7**, 11327 (2015).
[53] F. Bechstedt, K. Tenelsen, B. Adolph, and R. Del Sole, Phys. Rev. Lett. **78**, 1528 (1997).
[54] A. Marini and R. Del Sole, Phys. Rev. Lett. **91**, 176402 (2003).
[55] A. Marini, J. Phys.: Conf. Ser. **427**, 012003 (2013).
[56] M. Bernardi, D. Vigil-Fowler, J. Lischner, J. B. Neaton, and S. G. Louie, Phys. Rev. Lett. **112**, 257402 (2014).
[57] B. D. Malone and E. Kaxiras, Phys. Rev. B **87**, 245312 (2013).
[58] X. Ling, S. Huang, E. H. Hasdeo, L. Liang, W. M. Parkin, Y. Tatsumi, A. R. T. N. A. A. Puretzky, P. M. Das, B. G. Sumpter, D. B. Geohegan, J. Kong, R. Saito, M. Drndic, V. Meunier, and M. S. Dresselhaus, Nano Lett. **16**, 2260 (2016).
[59] S. Logothetidis, L. Vinna, and M. Cardona, Phys. Rev. B **31**, 2180 (1985).
[60] G. Antonius, S. Poncé, P. Boulanger, M. Côté, and X. Gonze, Phys. Rev. Lett. **112**, 215501 (2014).
[61] S. Zhang, N. Wang, S. Liu, S. Huang, W. Zhou, B. Cai, M. Xie, Q. Yang, X. Chen, and H. Zeng, Nanotechnology **27**, 274001 (2016).